# Ultrabroadband and band-selective thermal meta-emitters by machine learning

https://doi.org/10.1038/s41586-025-09102-y

Received: 1 December 2024

Accepted: 6 May 2025

**Chengyu Xiao[1,2], Mengqi Liu[3,4], Kan Yao[5], Yifan Zhang[1,2], Mengqi Zhang[1,2], Max Yan[6], Ya Sun[1,2,3], Xianghui Liu[1], Xuanyu Cui[1,2], Tongxiang Fan[1], Changying Zhao[4], Wansu Hua[1,2], Yinqiao Ying[1,2], Yuebing Zheng[5,7]✉, Di Zhang[1]✉, Cheng-Wei Qiu[3,8]✉ & Han Zhou[1,2]✉**

Thermal nanophotonics enables fundamental breakthroughs across technological applications from energy technology to information processing[1–11]. From thermal emitters to thermophotovoltaics and thermal camouflage, precise spectral engineering has been bottlenecked by trial-and-error approaches. Concurrently, machine learning has demonstrated its powerful capabilities in the design of nanophotonic and meta-materials[12–18]. However, it remains a considerable challenge to develop a general design methodology for tailoring high-performance nanophotonic emitters with ultrabroadband control and precise band selectivity, as they are constrained by predefined geometries and materials, local optimization traps and traditional algorithms. Here we propose an unconventional machine learning-based paradigm that can design a multitude of ultrabroadband and band-selective thermal meta-emitters by realizing multiparameter optimization with sparse data that encompasses three-dimensional structural complexity and material diversity. Our framework enables dual design capabilities: (1) it automates the inverse design of a vast number of possible metastructure and material combinations for spectral tailoring; (2) it has an unprecedented ability to design various three-dimensional meta-emitters by applying a three-plane modelling method that transcends the limitations of traditional, flat, two-dimensional structures. We present seven proof-of-concept meta-emitters that exhibit superior optical and radiative cooling performance surpassing current state-of-the-art designs. We provide a generalizable framework for fabricating three-dimensional nanophotonic materials, which facilitates global optimization through expanded geometric freedom and dimensionality and a comprehensive materials database.

Thermal emission is a fundamental feature of nature. Nanophotonic engineering is used to tailor the spectrum, directionality and polarization of thermally emitted light, with a broad range of applications[3–11]. For each application, the ideal spectral profiles of thermal emitters must be carefully designed to accommodate variations in settings, whether extraterrestrial or terrestrial[2], atmospheric conditions[19,20], operational temperatures[11] or humidity levels[2] (Supplementary Fig. 1). For example, it is essential for a band-selective thermal emitter to exhibit near-unity emissivity in the transparent atmospheric window and near-unity reflectance at non-atmospheric-window wavelengths for terrestrial, subambient, passive cooling[21,22] and for mitigating the urban heat-island effect[7]. Conversely, a broadband emitter with high emissivity across the entire mid-infrared waveband is crucial for daytime above-ambient cooling[23,24] and for extraterrestrial applications[25]. Consequently, the design of thermal emitters necessitates the optimization of thermal emission bandwidths, band positions and numbers, along with simultaneous control across the ultraviolet to infrared spectrum[22,24]. Previously reported emitters have been limited and were mostly based on previous empirical or physics-based knowledge using trial-and-error[2]. A general design methodology is, therefore, essential for the efficient and precise design of customized emitters with the desired spectral profiles.

Artificial intelligence, particularly machine learning (ML), has revolutionized and dramatically speeded up the design of nanophotonic and meta-materials[12–18,26–28]. However, two substantial challenges persist. One challenge is the lack of automated inverse design methods capable of simultaneously achieving global optimization across diverse structures and several materials. Traditional optimization techniques, such as gratings[29], multilayers[30–32] and predominantly simple metastructures[17,33–36], are constrained by a set of predefined geometries and materials, which restricts their capacity for multistructure and

---

[1]State Key Laboratory of Metal Matrix Composites, School of Materials Science and Engineering, Shanghai Jiao Tong University, Shanghai, P. R. China. [2]Future Materials Innovation Center, Zhangjiang Institute for Advanced Study, Shanghai Jiao Tong University, Shanghai, P. R. China. [3]Department of Electrical and Computer Engineering, National University of Singapore, Singapore, Singapore. [4]Institute of Engineering Thermophysics, MOE Key Laboratory for Power Machinery and Engineering, School of Mechanical Engineering, Shanghai Jiao Tong University, Shanghai, P. R. China. [5]Materials Science and Engineering Program and Texas Materials Institute, The University of Texas at Austin, Austin, TX, USA. [6]Department of Applied Physics and Electronics, Umeå University, Umeå, Sweden. [7]Walker Department of Mechanical Engineering, The University of Texas at Austin, Austin, TX, USA. [8]Nanotech Energy and Environment Platform, National University of Singapore, Suzhou Research Institute, Suzhou, P. R. China. ✉e-mail: zheng@austin.utexas.edu; zhangdi@sjtu.edu.cn; chengwei.qiu@nus.edu.sg; hanzhou_81@sjtu.edu.cn

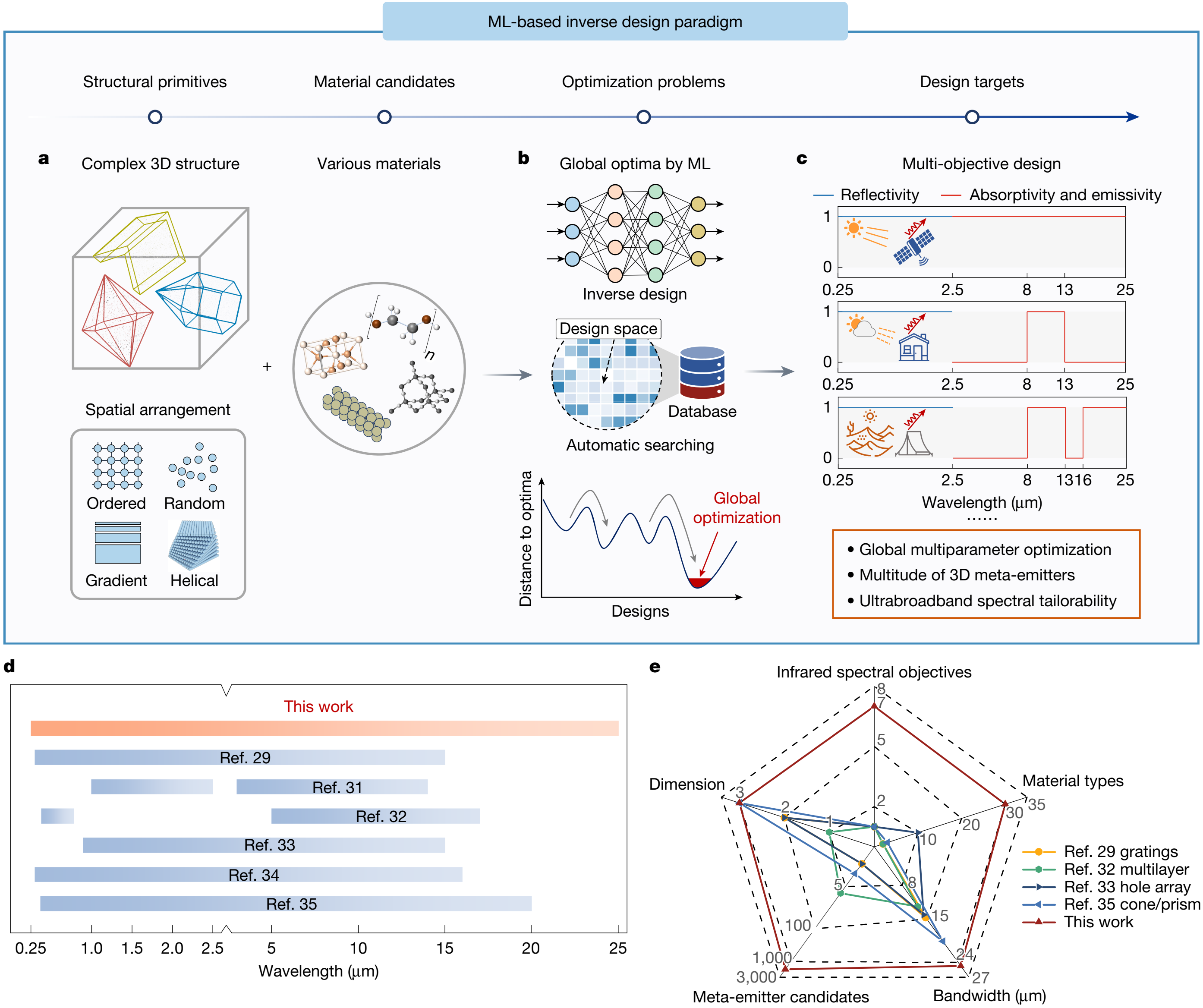

**Fig. 1 | ML-based general inverse design paradigm.** **a**, The proposed ML-based approach incorporates 3D structural primitives and spatial arrangements (left) and a database of diverse candidate materials (right). **b**, It has the potential to deliver global optimization solutions. **c**, The method can feasibly meet multi-objective and customer-specific spectral demands. **d**, Design wavelength range compared to previous ML-based studies. **e**, Comparison of design space coverage for this work and previous ML-based work, including the number of meta-emitter candidates, material diversity, bandwidth ranges and dimensions in a simultaneous multi-objective optimization capability.

multiparameter optimization. Methods like genetic algorithms and simple ML algorithms[14] are prone to falling into local optimization traps[37]. These bottlenecks lead to limitations such as narrow bandwidths, restricted band selectivity and suboptimal photonic properties[13]. Consequently, there is a pressing need for global optimization that can leverage expanded geometric freedom and dimensionality and a comprehensive materials database to create high-performance, thermal, nanophotonic materials through a flexible spectral engineering capability.

A second challenge is encountered in the design of complex and diverse 3D photonic structures. Photonic engineering typically parameterizes features like length and thickness for simple geometric primitives[29–32]. However, traditional ML methods are predominantly limited to two-dimensional structures due to the absence of robust descriptive and parameterization techniques that can describe a multitude of higher-dimensional structures. Addressing these gaps necessitates the development of effective descriptors and algorithms that can describe various complex 3D photonic structures and handle computational complexity, which is a formidable challenge. To date, methodologies addressing these challenges remain elusive and have not yet been fully developed. Further development of general advanced optimization schemes will be pivotal in tackling such inverse design challenges.

We have developed an unconventional, general, ML-based paradigm for the multi-objective design and exploration of nanophotonic thermal emitters. It is the most extensive design platform for accurately designing a multitude of ultrabroadband and band-selective thermal meta-emitters (TMEs), and therefore, it can guide the inverse design of nanophotonic and meta-materials. Our approach offers three distinct advantages: (1) It has an automated platform for unprecedented global optimization using 3D structural primitives, spatial arrangements and a comprehensive materials dataset (Fig. 1a) in a vast parameter space (Fig. 1b). The algorithm has successfully designed over 1,500 types of meta-emitters exhibiting desired photonic properties. (2) We have established an approach for designing 3D photonic structures using a three-plane modelling method, which enhances design flexibility in terms of dimensionality and surpasses the limitations of traditional two-dimensional structures. (3) We have validated our findings in experiments that demonstrated the superior optical and radiative cooling performance of our TMEs compared to current state-of-the-art designs. This research may facilitate the straightforward identification of promising meta-emitters that have the potential for manufacturing scalability and practical applicability from diverse candidates.

## Overview of the inverse design paradigm

Our design approach diverges significantly from conventional empirical engineering methods (Supplementary Fig. 2). We concentrated on constructing an expansive, parameterized design space. By combining a powerful geometric/material descriptor with ML algorithms, our approach completes an exhaustive exploration across the design space, thus enabling effective inverse nanophotonic engineering. Three critical aspects of our framework merit consideration: (1) the comprehensive database features 3D structural primitives and spatial arrangement combinations (Fig. 1a, left); (2) selecting suitable materials (Fig. 1a, right) involves considering several factors, including the electronic bandgap, refractive index, and chemical and thermal stability; (3) a unified descriptor system translates complex 3D structural and material data into computational parameters, thereby maximizing design flexibility. Collectively, these elements expand the search range of the algorithm and enable the exploration of previously inaccessible parts of the design space.

The proposed design concept is general, and it leverages a vast library of 3D photonic structures and diverse material systems. Numerous functionalities and flexible spectral tailorability can be achieved through various geometric/material combinations (Fig. 1c). Our platform stands out from previous ML-based approaches due to its unique advantages. It has flexible and ultrabroadband multispectral tailorability from the ultraviolet to the mid-infrared (0.25–25 μm), as shown in Fig. 1d. It can automatically combine and tailor several 3D photonic structures and materials to produce the desired spectral characteristics, thus fulfilling concurrent multi-objective design requirements (Fig. 1e).

## ML-based inverse design process and descriptors

A critical step was to develop effective, parameterized descriptors for both geometric and material properties. We compiled a comprehensive ‘library’ of structural primitives inspired by natural prototypes[38–43]—including spheres, cylinders, ridges and triangular prisms—along with their spatial arrangements (Supplementary Fig. 3 and Supplementary Table 1). These designs have evolved in biological systems, which exhibit diverse 3D hierarchical micro- and nanoscale structures with exceptional optical and thermal properties. Using our library, which comprises 32 basic 3D primitives (Fig. 2a and Supplementary Fig. 4), various spatial arrangements (Fig. 2b) and 30 candidate materials (Fig. 2d), our ML algorithm can generate tens of thousands of meta-emitter designs.

We initiated our ML process by defining a large design space with geometric and material information. We developed an efficient geometric/material descriptor capable of representing complex 3D hierarchical structures. Specifically, a three-plane modelling method was created to describe structural primitives (Fig. 2c). Each primitive is divided into three segments: a central plane (first plane), an upper plane (second plane) and a lower plane (third plane). Simple structures, such as hemispherical or cylindrical shapes, require only two planes, whereas more complex two-part structures necessitate all three planes, such as spherical, spherical-top cylinder and so on. Key parameters—such as size and shape—define the geometry of each plane, thus capturing the spherical, cylindrical or polygonal features as well as dimensions and edge length. Parameters for connection, distance, rotation and shelling (core-shell) further characterize the interrelationships between planes and the placement status of primitives. This three-plane method reduces each complicated 3D primitive to 11 essential variables, which enables the efficient mathematical encoding of typical 3D structural primitives (Supplementary Figs. 5 and 6). Additionally, spatial arrangements, including ordered, random and gradient (Fig. 2b), are described with displacement vectors (Supplementary Note 1 and Supplementary Fig. 7), yielding 37 parameters that fully encapsulate the 3D geometric information.

Subsequently, we selected materials based on their dielectric properties and developed a material descriptor for the ML process (Fig. 2d and Supplementary Note 2). To maximize solar reflectivity in the ultraviolet–visible–near-infrared range (0.25–2.5 μm), we evaluated 30 candidate materials with large electronic bandgaps and a high average refractive index ($n$) (Supplementary Fig. 8). For the infrared emissivity, we prioritized polymers and inorganic materials exhibiting phonon-polarization resonances to ensure absorption across the infrared band (3–25 μm) (Supplementary Table 2). The optical properties of each material were defined by its complex refractive index ($\tilde{n} = n + k\mathrm{i}$) (Supplementary Fig. 9). By integrating the material and geometric information about the structural primitives, we formulated a combined design descriptor (Fig. 2e and Supplementary Table 3), which captures the complex design space and enables global inverse design. This combined descriptor is the input to the prediction process of our ML framework. The outcomes are the solar reflectivity and infrared emissivity spectra (Supplementary Note 3).

## Training the algorithm platform

The ML-based design framework has four main steps (Fig. 2f): (1) establishing a database; (2) developing the forward prediction networks; (3) implementing an inverse design framework using a conditional generative adversarial network (Supplementary Note 4 and Supplementary Fig. 10); and (4) validating it through simulations and experiments. We constructed a comprehensive dataset of 57,110 randomly generated meta-emitters with details of structural primitives, spatial arrangements, constituent materials and spectral responses (Supplementary Fig. 11). To enhance data quality, we employed the Kennard–Stone algorithm to select a representative, uniformly distributed subset of 32,207 samples, allocating 70% for training and 30% for testing. This preprocessing minimized the overfitting risk by ensuring we used a diverse sample distribution, which bolstered the generalizability and predictive accuracy of the model[44] (Supplementary Fig. 12).

Because of the dimensional mismatch between geometric and material information, using raw design vectors could hinder training. To solve this, we applied autoencoders for dimensional reduction of both design and response vectors before inputting them into a fully connected neural network for forward prediction (Supplementary Table 4), which improved the accuracy over raw data (Supplementary Fig. 12). However, challenges in achieving an accurate inverse design arose from the different convergence rates of the discriminator and generator in the conditional generative adversarial network. To address this, we pretrained the generator, introduced 10% dataset perturbations and applied a weighted loss function to synchronize the training speeds (Supplementary Note 5 and Supplementary Fig. 13).

## Inverse multi-objective design of TMEs

To verify the design capabilities of our framework, we developed seven distinct TMEs tailored to specific applications (Supplementary Fig. 14): (1) TME-1 is a broadband meta-emitter has high emissivity across infrared wavelengths (3–25 μm) for above-ambient radiative cooling or extraterrestrial applications[23,24]; (2) TME-2 is a band-selective meta-emitter with peak emissivity in the first atmospheric window (8–13 μm) for terrestrial subambient radiative cooling[2]; (3) TME-3 is

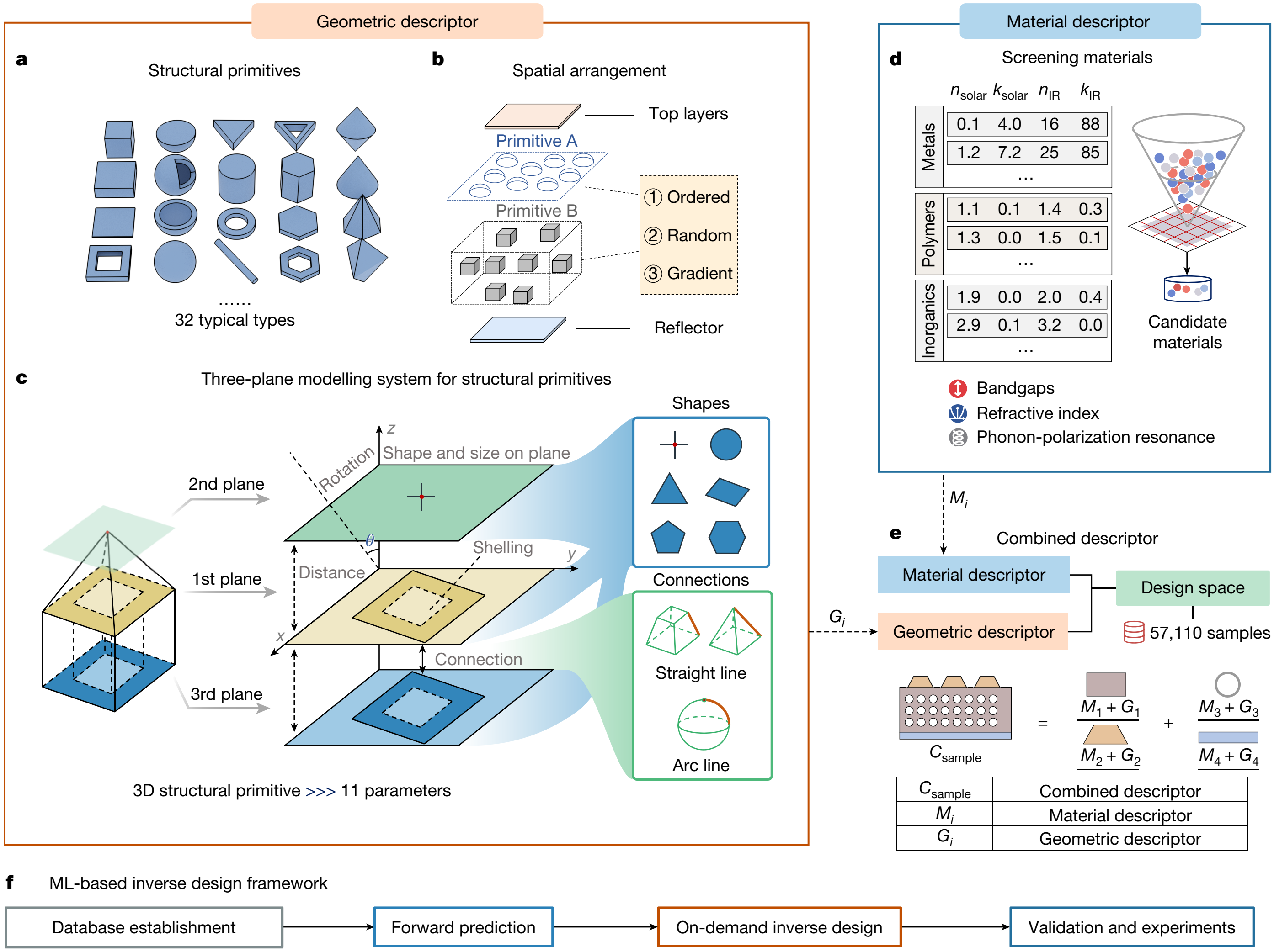

**Fig. 2 | ML-based inverse design process and descriptors. a**, Structural primitives derived from natural prototypes. **b**, Spatial arrangement of structural primitives. Primitive A lies above a substrate, and primitive B is embedded in the substrate. There is a top multilayer and a bottom reflecting layer. This holistic representation encompasses a wide range of photonic structures, from 1D to 3D hierarchical architectures. **c**, A three-plane modelling system developed to describe complex 3D geometries as the inputs. A structural primitive (left) is divided into three parallel sheets. Its features are projected onto the three planes, including shape, size and interplanar distance, as discrete descriptions of the primitive. **d**, Materials screening considers the bandgap, refractive index and phonon-polarization resonance. The ML inputs are the refractive indices ($n$) and extinction coefficients ($k$). $n_{\text{solar}}$, $k_{\text{solar}}$, $n_{\text{IR}}$ and $k_{\text{IR}}$ denote the $n$ and $k$ values in the solar and infrared bands, respectively. **e**, The design space is defined by combined geometric/material descriptors, yielding a training dataset of 57,110 samples and covering all features of the two primitive sets, substrate, reflector and top layers. Note that the latter two components are optional. **f**, The four main steps in the ML design framework.

a dual-band-selective meta-emitter with high emissivity across two atmospheric windows (8–13 and 16–25 μm)[19]; (4) TME-4 is a thermal camouflage meta-emitter with low emissivity within ranges 3–5 and 8–13 μm and high emissivity outside the atmospheric window (5–8 μm)[11]; (5) TME-5 is a two-sided Janus meta-emitter for daytime subambient cooling with a broadband high-emissivity side and for night-time supra-ambient warming with the low-emissivity side; (6) TME-6 and TME-7 are meta-emitters with customized spectra. Leveraging the processing capabilities of our trained conditional generative adversarial network could provide appropriate meta-emitter candidates for any requested spectrum and predict their performance metrics.

For each TME, we generated 2,000 models, screened to a 0.15 threshold (Supplementary Note 6), resulting in 545, 270, 121, 197, 146, 171 and 91 qualified designs, respectively, all meeting the spectral targets (Supplementary Figs. 16–18). We further validated 21 representative designs using finite-difference time-domain simulations (Fig. 3a and Supplementary Fig. 19). Notably, our methodology yielded a variety of hierarchical metastructures, including both conventional configurations (for example, photonic crystals and multilayered stacks) and previously unidentified designs that go beyond traditional empirical intuition (Fig. 3b and Supplementary Figs. 20–26). Furthermore, the framework can generate 2,500 candidates per second, vastly outpacing conventional optimization techniques (Supplementary Fig. 27).

We further analysed material and structural utility across wavelengths, which revealed clusters based on ML-identified physical laws (Fig. 3c). Although this analysis does not exhaust all potential possibilities, it illustrates that our framework can extract physical principles from complex datasets in the design of meta-emitters. This clustering aids in targeting subcategories of materials and structures without compromising optical responses, thus empowering viable designs tailored to specific spectral and stability requirements. For instance, for TME-1–TME-3, solutions can be visualized by auxiliary lines on the data graph, which streamlines the material and structural selection. Furthermore, using our automated selection algorithm and a relatively large

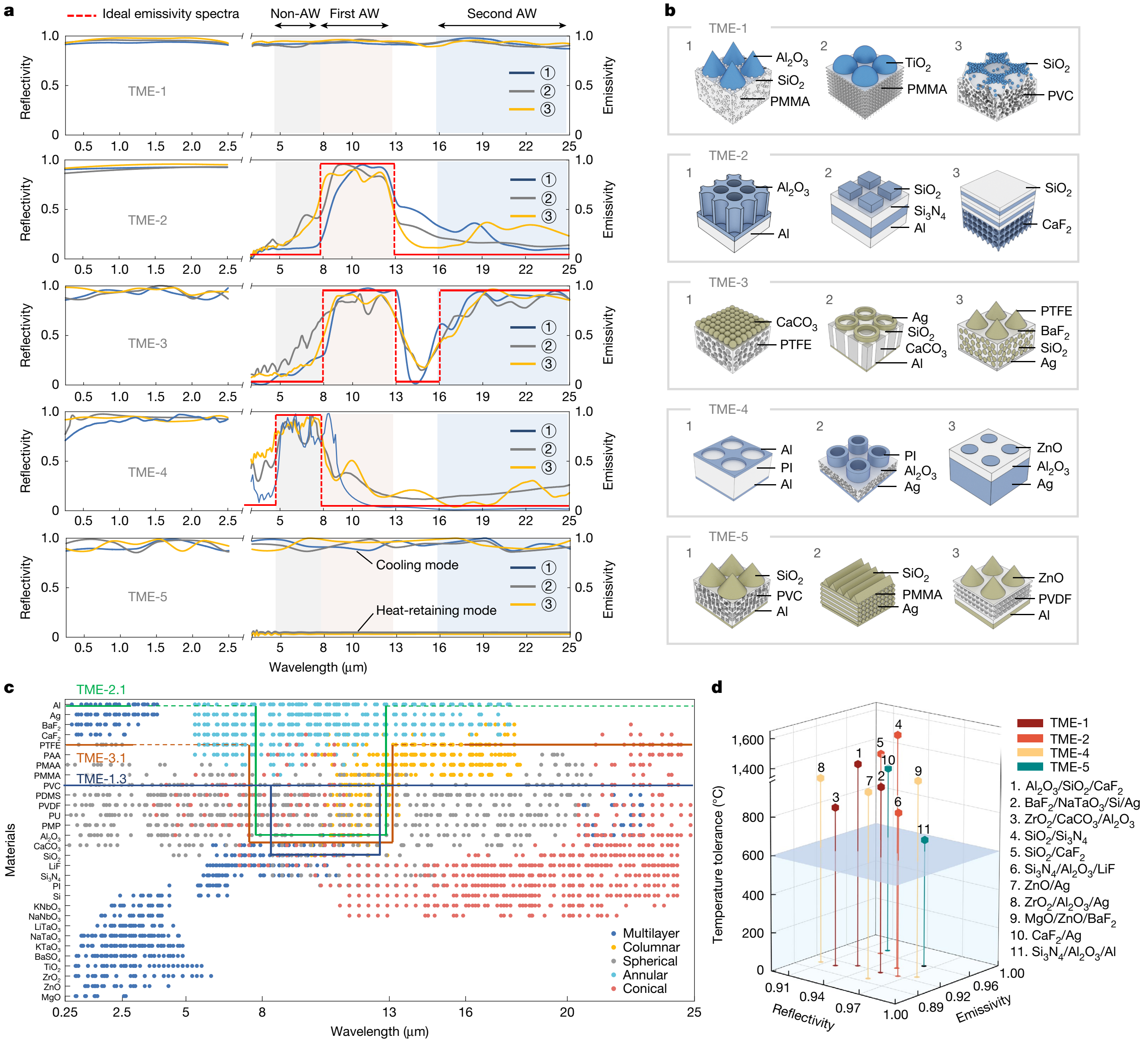

**Fig. 3 | Inverse design of different TMEs. a**,**b**, Spectra (**a**) and schematic diagrams (**b**) of three different designs for each TME task. For TME-5, high (low) emissivity corresponds to cooling (heat-retaining) mode (Supplementary Fig. 15). **c**, Relationships among materials, structural primitives and response wavelengths from an analysis of our results. The number of random input spectra was 24,000. Points represent high reflectivity (0.25–2.5 μm) and high emissivity (3–25 μm). The typical TME-1–TME-3 designs conform well to the pattern shown in the diagram (blue, green and brown lines). The dashed lines indicate omitted spectral regions. **d**, Several typical generated meta-emitters with potential high-temperature tolerance capabilities and high optical properties. The blue rectangle is the isothermal surface at 600 °C. AW, atmospheric window; PAA, poly(acrylic acid); PMAA, poly(methacrylic acid); PMMA, poly(methyl methacrylate); PU, polyurethane; PMP, poly(methyl pentene).

pool of materials, we can efficiently identify high-temperature-tolerant meta-emitters that simultaneously meet stringent thermal stability requirements and desired optical performance criteria (Fig. 3d and Supplementary Table 5).

## Experiments and performance assessment

To validate our designs, we synthesized four representative meta-emitter designs (TME-1 to TME-4) for experimental demonstration (Fig. 4a–c and Supplementary Figs. 28–32). Notably, the measured spectra closely matched the predicted responses from our ML framework (Fig. 4d), confirming the precision and effectiveness of our algorithms. For instance, TME-1, a broadband meta-emitter, with detailed features in Fig. 3b (TME-1.3) and Fig. 4a, achieved a solar reflectance of over 0.96 in 0.25–2.5 μm and a broadband infrared emissivity of 0.92 across 3–25 μm (Fig. 4d, with underlying mechanisms in Supplementary Figs. 33 and 34). TME-2, a band-selective meta-emitter, has a bilayer structure (TME-2.1) (Figs. 3b and 4b). The porous $Al_2O_3$ enhances the absorptivity within the first atmospheric window through cavity resonances (Supplementary Fig. 35) while reflecting other wavelengths. Our experimental measurements confirmed a near-ideal hat-shaped emissivity spectrum (Fig. 4d), with a high solar reflectivity of 0.96 and

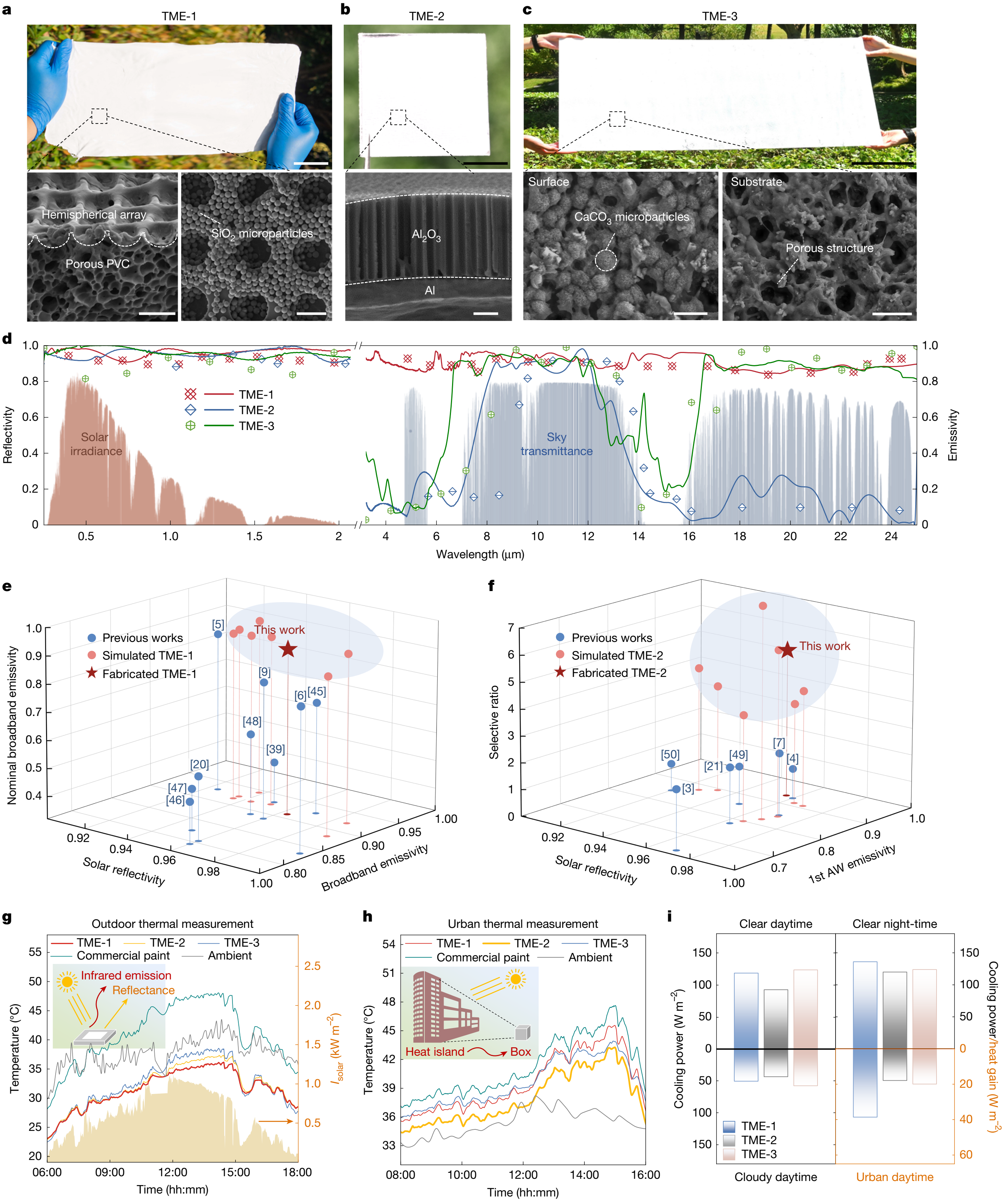

**Fig. 4 | Representative TMEs for proof-of-concept experimental validation and performance assessment. a**–**c**, Photographs (top) and scanning electron microscopy images (bottom) of the fabricated TME-1–TME-3. **a**, TME-1 is a bilayer film composed of porous PVC embedded with $Al_2O_3$ nanoparticles, with $SiO_2$ particles distributed on top. **b**, TME-2 is a thin film covered by a honeycomb-like porous array of $Al_2O_3$. **c**, TME-3 is composed of a porous PTFE film coated with $CaCO_3$ particles. **d**, Predicted (scatter plots) and measured (lines) reflectivity and emissivity of the designed TMEs. **e**,**f**, Comparisons of emissivity, solar reflectivity and wavelength tailorability between the generated TME-1 (**e**) and TME-2 (**f**) and other state-of-the-art systems. **g**, Daytime continuous measurement of the subambient radiative cooling performance on 18 July 2024 in Shanghai (31° 24′ 19″ N, 121° 29′ 22″ E), with solar intensities ($I_{solar}$) reaching up to 1,150 W m$^{-2}$. **h**, Temperatures of different samples measured in an urban heat-island set-up on 23 July 2024. **i**, Calculated cooling power and heat gain across various scenarios for TME-1 to TME-3. Scale bars, 5 cm (**a**, top), 5 μm (**a**, bottom), 2 cm (**b**, top), 1 μm (**b**, bottom), 20 cm (**c**, top), 2 μm (**c**, bottom).

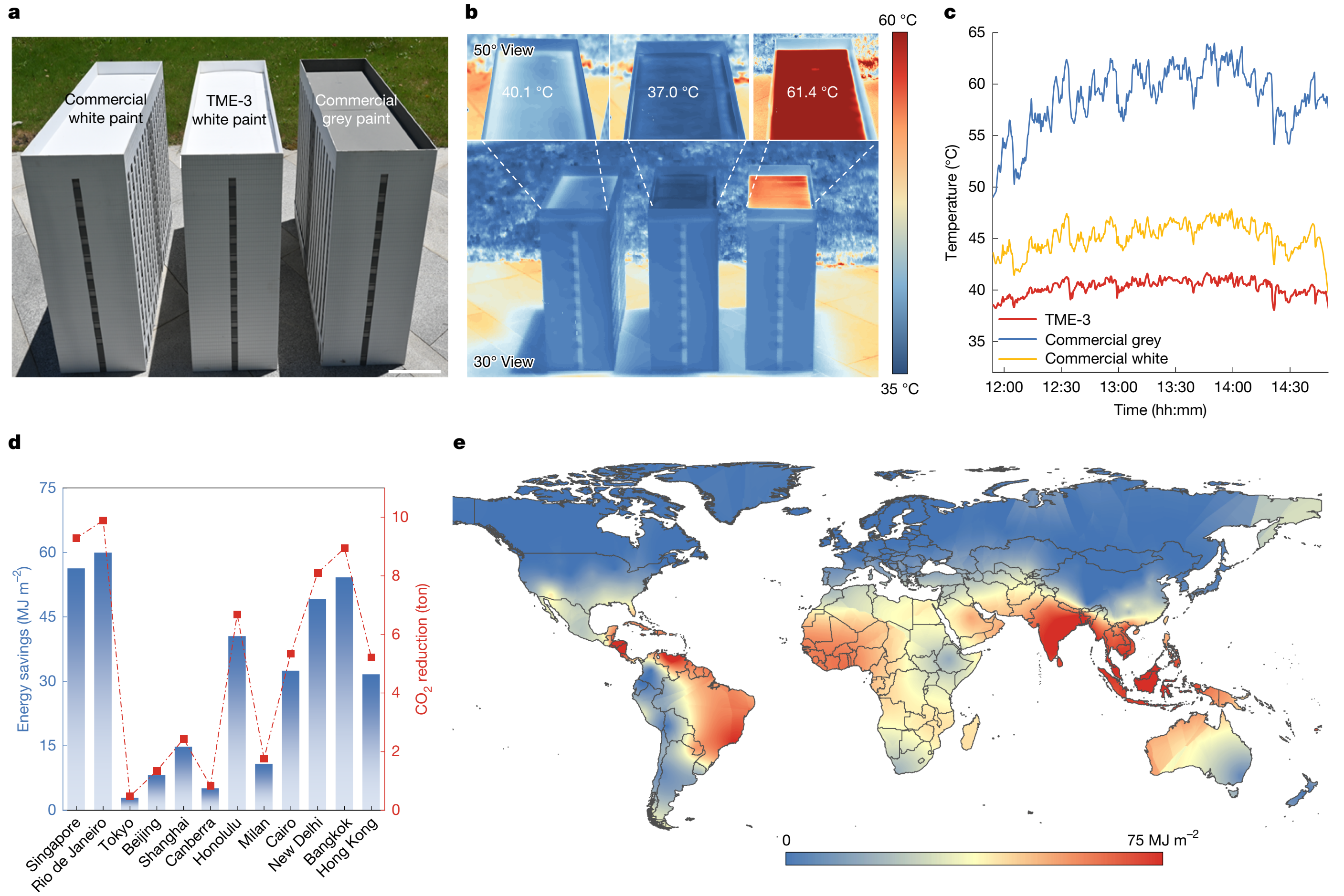

**Fig. 5 | Application and energy-saving evaluation for building envelopes.** **a**, Photograph of model houses with a TME-3 coating (middle) and white or grey commercial paint on the roof. **b**, Thermal images of the models after 30 min exposure to solar irradiance of up to 1,010 W m$^{-2}$. **c**, Thermocouple-recorded temperatures of the model houses. **d**, Calculated annual energy savings and CO$_2$ emission reductions (in tonnes) for a standard midrise apartment building after the TME-3 coating has been applied on the roof. **e**, Our projected global estimate of energy savings, considering both cooling and heating energy consumption. Scale bar in **a**, 20 cm. Colour bars indicate apparent temperature (**b**) and energy savings (**e**).

an average emissivity of 0.92 across the first atmospheric window. TME-3, a dual-band-selective meta-emitter, with detailed features in Fig. 3b (TME-3.1) and Fig. 4c, displayed exceptional optical properties, including emissivity reaching up to 0.95 in the first atmospheric window (8–13 μm) and 0.90 in the second atmospheric window (16–25 μm), while maintaining a high reflectance in the remaining mid-infrared and solar bands. The high dual-band-selective emissivity is attributed to the absorption bands of CO$_3^{2-}$ (875–1,425 cm$^{-1}$) and C–F bonds (400–540 cm$^{-1}$) in polytetrafluoroethylene (PTFE) (Supplementary Table 2). The solar reflectivity was enhanced by Mie scattering of CaCO$_3$ spheres and the micro- and nanopores within the PTFE substrate.

To quantitatively assess the multispectral wavelength tailorability, we introduced two metrics: the nominal broadband emissivity $\eta$, which is a measure of the broadband-emissive characteristics of TME-1, and the selective ratio $\gamma$, which is a measure of the band selectivity of TME-2 (Methods)[7]. Notably, our ML-based approach efficiently generates a great quantity of TME designs with excellent optical performance that surpasses their state-of-the-art material counterparts in terms of solar reflectivity, emissivity and wavelength tailorability, as compared in Fig. 4e,f and Supplementary Fig. 36. Notably, TME-1 demonstrated near-unity nominal broadband emissivity, affirming the ultrabroadband optimization capabilities of our approach compared with methods in other works[5,6,9,20,39,45–48] (Fig. 4e and Supplementary Table 6). Moreover, TME-2 achieved a selective ratio of up to 5.52, which is 2 times higher than typical values reported so far[3,4,7,21,49,50] (Fig. 4f and Supplementary Table 6). These results underscore the ability of the ML approach to meet stringent spectrum engineering requirements for ultrabroadband, mono-selective or dual-selective applications.

We experimentally evaluated the terrestrial radiative cooling performance of TME-1, 2 and 3 under various application scenarios, focusing on weather conditions including ambient temperature, relative humidity and ground temperature. In outdoor measurements, all three meta-emitters maintained subambient temperatures (Fig. 4g), but their distinct emission spectra led to different cooling behaviours. Under clear skies, TME-1 achieved a significant temperature drop of 5.9 °C at midday due to reduced atmospheric water vapour, which reduced the heat load from counter radiation outside the atmospheric windows. However, cloudy conditions increased the absorption of counter radiation, which reduced the efficiency of TME-1 (Supplementary Fig. 37), whereas TME-2, with its band-selective emission, achieved a 4.6 °C subambient drop. In urban scenarios (vertically placed facing a wall; Fig. 4h and Supplementary Fig. 38), TME-2 achieved superior performance, maintaining temperatures 2.5 and 5.3 °C lower than TME-1 and commercial white paint, respectively (Fig. 4h). This is attributed to its ability to emit heat while selectively blocking unwanted thermal radiation from the surroundings (maximum of approximately 70 °C).

We conducted an in-depth analysis of the cooling power under various scenarios: clear days, cloudy days and urban environments (Fig. 4i and Supplementary Note 7). Under clear daytime conditions, TME-1 and TME-3 exhibited higher cooling powers of approximately 120 W m$^{-2}$, so that they efficiently dissipated heat into space with minimal interference from water vapour and clouds. By contrast, under cloudy conditions, the transmittance of the atmospheric windows was significantly reduced due to increased water vapour concentration, resulting in a substantial decline in the net cooling power (Supplementary Fig. 39). In urban environments, TME-2 outperformed both TME-1 and TME-3 with an obviously lower heat gain because of its spectral selectivity.

For extraterrestrial applications, TME-1 proved particularly well suited for deployment in such extreme environments, due to its ability to reflect nearly all solar irradiation while maximizing infrared emission[24]. Moreover, it has considerable operational stability (Supplementary Fig. 40). Details of this theoretical CubeSat study are provided in Supplementary Note 8 and Supplementary Fig. 41.

## Applicability and energy-saving evaluation

Drawing from thousands of generated models, we can easily identify meta-emitters that meet manufacturability criteria for large-scale production (Supplementary Tables 7–12). For instance, TME-3 can be applied easily, just like using paint (Supplementary Fig. 42), and its room-temperature and solution-based fabrication can be used to coat various surfaces like bricks, metals, plastics and glass (Supplementary Fig. 43). To evaluate its practical cooling effect, we constructed three identical model houses (Fig. 5a,b). Real-world thermal profiling during peak solar irradiance (4-hour midday monitoring period) demonstrated that the TME-3-coated roof surface maintained temperatures 5.6 °C below conventional white paint and 21 °C under standard grey-coated benchmarks (Fig. 5c). This highlights its practical potential for urban heat mitigation and, thereby, improving habitability in a hot climate. To evaluate the potential reduction in electricity and $CO_2$ emissions on a larger scale, we simulated the energy consumption of a typical four-storey midrise apartment building with a TME-3-coated roof (Supplementary Fig. 44). Considering the energy used by heating, ventilation and air-conditioning systems, the application of TME-3 as an external envelope material demonstrated impressive energy-saving performance in the selected cities, particularly in tropical regions (Fig. 5d and Supplementary Figs. 45–47). In extreme hot climates, the annual energy savings for indoor air-conditioning could reach up to 75 MJ $m^{-2}$, equivalent to 57.2 GJ (approximately 15,800 kWh) per year (Fig. 5e). Furthermore, the versatile applications for TME-3 include sunshades, textiles and coloured wearables (Supplementary Figs. 48–50).

## Conclusions

We have developed a general design platform integrating machine intelligence, computational simulation and experimental validation to autonomously discover and optimize a diverse family of TMEs. This framework not only achieves an exponential expansion of the thermal metamaterial design space but also enables fundamental advances in nanoscale light–matter interactions. Through precise spectral engineering, we have developed materials ready for scalable deployment across diverse infrastructure applications. Our generalized ML-driven framework, which has enlarged the design space for global TME designs, is key to the next paradigm shift in inverse design. When more structural primitives, spatial arrangements and materials features are included, this workflow will probably be applicable to a wide range of nanophotonic materials, with capabilities extending to coloured meta-emitters (Supplementary Fig. 51), meta-optics, topological photonics and beyond.

## Online content

Any methods, additional references, Nature Portfolio reporting summaries, source data, extended data, supplementary information, acknowledgements, peer review information; details of author contributions and competing interests; and statements of data and code availability are available at https://doi.org/10.1038/s41586-025-09102-y.

1. Baranov, D. et al. Nanophotonic engineering of far-field thermal emitters. *Nat. Mater.* **18**, 920–930 (2019).
2. Yin, X., Yang, R., Tan, G. & Fan, S. Terrestrial radiative cooling: using the cold Universe as a renewable and sustainable energy source. *Science* **370**, 786–791 (2020).
3. Raman, A. P. et al. Passive radiative cooling below ambient air temperature under direct sunlight. *Nature* **515**, 540–544 (2014).
4. Zhai, Y. et al. Scalable-manufactured randomized glass-polymer hybrid metamaterial for daytime radiative cooling. *Science* **355**, 1062–1066 (2017).
5. Zeng, S. et al. Hierarchical-morphology metafabric for scalable passive daytime radiative cooling. *Science* **373**, 692–696 (2021).
6. Lin, K. et al. Hierarchically structured passive radiative cooling ceramic with high solar reflectivity. *Science* **382**, 691–697 (2023).
7. Wu, R. et al. Spectrally engineered textile for radiative cooling against urban heat islands. *Science* **384**, 1203–1212 (2024).
8. Mandal, J. et al. Hierarchically porous polymer coatings for highly efficient passive daytime radiative cooling. *Science* **362**, 315–319 (2018).
9. Li, T. et al. A radiative cooling structural material. *Science* **364**, 760–763 (2019).
10. Li, Y. et al. Structured thermal surface for radiative camouflage. *Nat. Commun.* **9**, 273 (2018).
11. Zhu, H. et al. Multispectral camouflage for infrared, visible, lasers and microwave with radiative cooling. *Nat. Commun.* **12**, 1805 (2021).
12. Yao, K. & Zheng, Y. *Nanophotonics and Machine Learning*, Vol. 241 (Springer, 2023).
13. Ma, W. et al. Deep learning for the design of photonic structures. *Nat. Photonics* **15**, 77–90 (2020).
14. Zhu, C. et al. Machine learning aided design and optimization of thermal metamaterials. *Chem. Rev.* **124**, 4258–4331 (2024).
15. Molesky, S. et al. Inverse design in nanophotonics. *Nat. Photonics* **12**, 659–670 (2018).
16. Ma, W. et al. Pushing the limits of functionality-multiplexing capability in metasurface design based on statistical machine learning. *Adv. Mater.* **34**, 2110022 (2022).
17. Liu, Z. et al. Generative model for the inverse design of metasurfaces. *Nano Lett.* **18**, 6570–6576 (2018).
18. Chen, J. et al. Correlating metasurface spectra with a generation-elimination framework. *Nat. Commun.* **14**, 4872 (2023).
19. Wu, X. et al. A dual-selective thermal emitter with enhanced subambient radiative cooling performance. *Nat. Commun.* **15**, 815 (2024).
20. Zhao, X. et al. A solution-processed radiative cooling glass. *Science* **382**, 684–691 (2023).
21. Li, D. et al. Scalable and hierarchically designed polymer film as a selective thermal emitter for high-performance all-day radiative cooling. *Nat. Nanotechnol.* **16**, 153–158 (2021).
22. Fan, S. & Li, W. Photonics and thermodynamics concepts in radiative cooling. *Nat. Photonics* **16**, 182–190 (2022).
23. Tang, H. et al. Both sub-ambient and above-ambient conditions: a comprehensive approach for the efficient use of radiative cooling. *Energy Environ. Sci.* **17**, 4498–4507 (2024).
24. Zhao, D. et al. Radiative sky cooling: fundamental principles, materials, and applications. *Appl. Phys. Rev.* **6**, 021306 (2019).
25. Lan, P. et al. Hierarchical ceramic nanofibrous aerogels for universal passive radiative cooling. *Adv. Funct. Mater.* **34**, 202410285 (2024).
26. Kim, M. J. et al. Deep learning-assisted inverse design of nanoparticle-embedded radiative coolers. *Opt. Express* **32**, 16235–16247 (2024).
27. Guan, Q. et al. Machine learning-enabled inverse design of radiative cooling film with on-demand transmissive color. *ACS Photonics* **10**, 715–726 (2023).
28. Ding, Z. et al. Machine-learning-assisted design of a robust biomimetic radiative cooling metamaterial. *ACS Mater. Lett.* **6**, 2416–2424 (2024).
29. Seo, J. et al. Design of a broadband solar thermal absorber using a deep neural network and experimental demonstration of its performance. *Sci. Rep.* **9**, 15028 (2019).
30. Yu, S. et al. General deep learning framework for emissivity engineering. *Light: Sci. Appl.* **12**, 291 (2023).
31. Jiang, X. et al. Implementing of infrared camouflage with thermal management based on inverse design and hierarchical metamaterial. *Nanophotonics* **12**, 1891–1902 (2023).
32. Xi, W. et al. Ultrahigh-efficient material informatics inverse design of thermal metamaterials for visible-infrared-compatible camouflage. *Nat. Commun.* **14**, 4694 (2023).
33. Liu, X. et al. Compatible stealth metasurface for laser and infrared with radiative thermal engineering enabled by machine learning. *Adv. Funct. Mater.* **33**, 2212068 (2023).
34. Sullivan, J., Mirhashemi, A. & Lee, J. Deep learning-based inverse design of microstructured materials for optical optimization and thermal radiation control. *Sci. Rep.* **13**, 7382 (2023).
35. Su, W. et al. Machine learning-enabled design of metasurface based near-perfect daytime radiative cooler. *Sol. Energy Mater. Sol. Cells* **260**, 112488 (2023).
36. Ma, W. et al. Probabilistic representation and inverse design of metamaterials based on a deep generative model with semi-supervised learning strategy. *Adv. Mater.* **31**, 1901111 (2019).
37. Kudyshev, Z., Kildishev, A. V., Shalaev, V. M. & Boltasseva, A. Machine-learning-assisted metasurface design for high-efficiency thermal emitter optimization. *Appl. Phys. Rev.* **7**, 021407 (2020).
38. Shi, N. N. et al. Keeping cool: enhanced optical reflection and radiative heat dissipation in Saharan silver ants. *Science* **349**, 298–301 (2015).
39. Zhang, H. et al. Biologically inspired flexible photonic films for efficient passive radiative cooling. *Proc. Natl Acad. Sci. USA* **117**, 14657–14666 (2020).
40. Jordan, T. M., Partridge, J. C. & Roberts, N. W. Non-polarizing broadband multilayer reflectors in fish. *Nat. Photonics* **6**, 759–763 (2012).
41. Lemcoff, T. et al. Brilliant whiteness in shrimp from ultra-thin layers of birefringent nanospheres. *Nat. Photonics* **17**, 485–493 (2023).

42. Tsai, C. C. et al. Physical and behavioral adaptations to prevent overheating of the living wings of butterflies. *Nat. Commun.* **11**, 551 (2020).
43. Choi, S. H. et al. Anderson light localization in biological nanostructures of native silk. *Nat. Commun.* **9**, 452 (2018).
44. Morais, C. L. M. et al. Standardization of complex biologically derived spectrochemical datasets. *Nat. Protoc.* **14**, 1546–1577 (2019).
45. Huang, M. et al. A hierarchically structured self-cleaning energy-free polymer film for daytime radiative cooling. *Chem. Eng. J.* **442**, 136239 (2022).
46. Zhou, M. et al. Vapor condensation with daytime radiative cooling. *Proc. Natl Acad. Sci. USA* **118**, e2019292118 (2021).
47. Yang, Z. & Zhang, J. Bioinspired radiative cooling structure with randomly stacked fibers for efficient all-day passive cooling. *ACS Appl. Mater. Interfaces* **13**, 43387–43395 (2021).
48. Shi, S. et al. Scalable bacterial cellulose-based radiative cooling materials with switchable transparency for thermal management and enhanced solar energy harvesting. *Small* **19**, 202301957 (2023).
49. Zhao, D. et al. Subambient cooling of water: toward real-world applications of daytime radiative cooling. *Joule* **3**, 111–123 (2019).
50. Xu, Y. et al. Multiscale porous elastomer substrates for multifunctional on-skin electronics with passive-cooling capabilities. *Proc. Natl Acad. Sci. USA* **117**, 205–213 (2020).

# Methods

## Fabrication of TMEs

TME-1 was prepared using a template method (Supplementary Fig. 29). The fabrication began with cleaning a silicon wafer using a 150-W oxygen plasma for 300 s, followed by spin-coating a 1.2-μm-thick positive photoresist at 2,500 rpm for 60 s and hard-baking at 100 °C for 90 s. The wafer was then aligned with a photomask, exposed to ultraviolet light for 15 s using a proximity lithography system (SUSS MA8/BA8), developed in a tetramethyl ammonium hydroxide solution for 45 s and rinsed. Reactive ion etching with sulfur hexafluoride ($SF_6$) was employed to form a hemispherical pore structure and complete the silicon mould. To facilitate demoulding, the mould was treated with 1H,1H,2H,2H-perfluorodecyltriethoxysilane (Macklin H817036) for 30 min. A degassed polydimethylsiloxane (PDMS) solution (Supelco 57928-U), prepared with a curing agent in a 1:12 (v/v) ratio, was poured onto the silicon mould and cured at 60 °C for 3 h, yielding the PDMS template. Polyvinyl chloride (PVC, *K* value 62–60) particles (16 wt%) were then dispersed into a 45 °C N,N-dimethylformamide (DMF) solution under continuous stirring, cast onto the PDMS template and left to solidify in air such that air-induced phase separation resulted in a porous structure. Finally, the structured PVC composite was briefly immersed in a 5% aqueous DMF solution containing silica ($SiO_2$) microparticles (1 μm in diameter) floating on the liquid surface and left for 10–15 s to allow slight dissolution of the surface microstructure, leading to the spontaneous firm adsorption of $SiO_2$ onto the PVC surface, thereby forming the final TME-1 sample. Owing to the high accessibility of PDMS templates, splicing technology can be used to fabricate large TME-1 films.

The free-standing band-selective TME-2 was fabricated using two-step anodization (Supplementary Fig. 30). High-purity aluminium foil (Al, 99.999%, Macklin, thickness of 0.5 mm) was first cleaned sequentially in acetone, ethanol and deionized water, followed by electrochemical polishing in a perchloric acid ($HClO_4$) and ethanol solution (1:4 v/v) at 20 V for 5 min to ensure a smooth surface. The first anodization was conducted in a 0.3 M oxalic acid solution at 2 °C under a d.c. voltage of 125 V for 8 h, forming a disordered porous alumina ($Al_2O_3$) layer, which was subsequently removed by chemical etching in a solution containing 6 wt% phosphoric acid ($H_3PO_4$) and 1.8 wt% $HClO_4$ at 60 °C for 50 min. A second anodization was then performed under identical conditions for 6 h, yielding a well-ordered porous alumina ($Al_2O_3$) structure with an initial pore diameter of approximately 240 nm. To achieve the target pore size, the sample underwent pore widening in 5 wt% $H_3PO_4$ at 30 °C for 60 min, resulting in a final structure with uniform hexagonally arranged pores of larger diameter, thus forming the desired band-selective TME-2.

The TME-3 film was also prepared by an air-induced phase separation method (Supplementary Fig. 31). First, low-density polyvinylidene fluoride (PVDF) was dissolved in DMF at 45 °C under stirring to form a homogeneous dilute solution with a concentration of 3 g per 100 ml. The PVDF functioned as a binder. To preserve the band selectivity, the concentration of PVDF had to be maintained at a minimum level. After standing for 3 h, calcium carbonate ($CaCO_3$) microparticles (diameter of approximately 2 μm) and PTFE nano-powders (diameter of less than 30 nm) were added to the solution in ratios of 10.1 g per 100 ml and 4.5 g per 100 ml, respectively, followed by stirring at 45 °C to ensure uniform dispersion. The slurry-like TME-3 precursor solution can be deposited with several different coating methods (spin, spray or brush coating), depending on viscosity, to facilitate the formation of a film on various substrates such as metal, glass or brick. To mitigate shrinkage, the film was coated in a cool environment at 20 °C and allowed to dry under ambient conditions for 24 h. During this process, phase separation occurred, resulting in the formation of a porous structure. Notably, $CaCO_3$ microparticles exhibited spontaneous surface aggregation, whereas the PTFE was uniformly and densely distributed as the primary component within the porous matrix. A TME-3 film was obtained on completion of drying.

The TME-4 film was fabricated using a lift-off process (Supplementary Fig. 32). First, a phosphorus-doped silicon (100) wafer was cleaned with oxygen plasma to remove organic contaminants. A 100-nm-thick aluminium layer and a 720-nm-thick silicon layer were sequentially deposited onto the substrate by electron beam evaporation. Next, a layer of positive photoresist was spin-coated onto the sample and soft-baked. Ultraviolet lithography was performed using a quartz mask, followed by immersion in a wet developer to define the desired pattern. The developed sample was then hard-baked at 100 °C to enhance stability. Afterward, 75 nm of aluminium was deposited by thermal evaporation. The lift-off process was carried out by placing the sample in an acetone solution within a 45 °C water bath for 20 min to dissolve the photoresist and remove excess aluminium. Finally, ultrasonic treatment ensured the complete removal of residual contaminants to yield a well-defined TME-4 film structure.

## Simulation of optical properties

Full-wave simulations conducted by FDTD Solutions (Lumerical Co., Ltd) were used to calculate the reflectivity of the solar band (0.25–2.5 μm) and the absorptivity and emissivity within the infrared band (3–25 μm). The microstructural details were abstracted from biological prototypes (Supplementary Table 1) and recreated by three-plane geometric descriptors in MATLAB R2022b. The 3D structural units were assumed to be periodically arranged. Realistic optical properties (complex refractive indices) of common materials, obtained from measurements and open-access refractive index databases, were assigned to the basic geometries. The reflectivity and transmissivity were calculated by averaging the results for transverse-electric-polarized and transverse-magnetic-polarized light to account for the unpolarized incident light in experiments.

## Optical and morphological characterizations

The solar reflectivity was measured for the wavelength range 250–2,500 nm with an ultraviolet–visible–near-infrared spectrophotometer (PerkinElmer, Lambda 950). The infrared reflectivity *R* and transmissivity *T* were measured using a Fourier-transform infrared spectrometer (Thermal Scientific, Nicolet iS50) operated in the range 3–25 μm with a gold integrating sphere (Peak Technologies). The absorptivity *A* was determined as $A = 1 - R - T$. Optical images were taken using Nikon D610 (visible) and FLIR T630 (infrared) cameras. Scanning electron microscopy was done using TESCAN MIRA 3 scanning electron microscope and Zeiss Gemini 300 scanning electron microscope.

## Nominal broadband emissivity and selective ratio

The nominal broadband emissivity $\eta$ was calculated as the product of the bandwidth coefficient (actual bandwidth divided by the ideal bandwidth of 3–25 μm) and the average emissivity within the high-emissivity band:

$$\eta = \frac{\int_{\lambda_1}^{\lambda_2} \mathrm{d}\lambda}{\int_{3\,\mu\mathrm{m}}^{25\,\mu\mathrm{m}} \mathrm{d}\lambda} \frac{\int_{\lambda_1}^{\lambda_2} \varepsilon(\lambda)\,\mathrm{d}\lambda}{\int_{\lambda_1}^{\lambda_2} \mathrm{d}\lambda} = \frac{\int_{\lambda_1}^{\lambda_2} \varepsilon(\lambda)\,\mathrm{d}\lambda}{\int_{3\,\mu\mathrm{m}}^{25\,\mu\mathrm{m}} \mathrm{d}\lambda} \tag{1}$$

in which $\varepsilon(\lambda)$ is the emissivity at wavelength $\lambda$, and $\lambda_1$ and $\lambda_2$ are the start and end wavelengths of the design band, respectively. The selective ratio $\gamma$ was defined as the ratio of the average emissivity of the first atmospheric window[7] to the emissivity of the range outside the first atmospheric window (3–8 and 13–25 μm):

$$\gamma = \frac{\left(\int_{8\,\mu\mathrm{m}}^{13\,\mu\mathrm{m}} \varepsilon(\lambda)\,\mathrm{d}\lambda\right) \Big/ \left(\int_{8\,\mu\mathrm{m}}^{13\,\mu\mathrm{m}} \mathrm{d}\lambda\right)}{\left(\int_{3\,\mu\mathrm{m}}^{8\,\mu\mathrm{m}} \varepsilon(\lambda)\,\mathrm{d}\lambda + \int_{13\,\mu\mathrm{m}}^{25\,\mu\mathrm{m}} \varepsilon(\lambda)\,\mathrm{d}\lambda\right) \Big/ \left(\int_{3\,\mu\mathrm{m}}^{8\,\mu\mathrm{m}} \mathrm{d}\lambda + \int_{13\,\mu\mathrm{m}}^{25\,\mu\mathrm{m}} \mathrm{d}\lambda\right)} \tag{2}$$

### Outdoor and urban thermal measurements

The set-up for outdoor thermal measurement is shown in Supplementary Figs. 37 and 38. To measure the radiative cooling performance when facing towards sky, TME and control samples of 8 cm × 8 cm were cut and put into a box made of thermal insulating polystyrene foam (100 cm × 70 cm × 80 cm). For each sample, separate chambers were formed using polystyrene. The entire foam (except for the sample area) was covered by aluminium foil. A solar power radiation meter (TES-1333R) was used to record the local solar radiation. The relative humidity and ambient temperature were measured using a weather meter (Kestrel 5500). The real-time temperature was measured with multichannel dataloggers with K/T-type thermocouples. For urban heat-island thermal measurements, samples of size 6 cm × 6 cm were cut and put into the centre near one side of separate, dedicated thermal insulating polystyrene boxes (20 cm × 30 cm × 15 cm). These thermally insulated boxes were placed near a wall at the bottom of a 45° slope. The apparatus was placed on a light-coloured trestle with a height of 80 cm to prevent conduction from the ground, which was at 70 °C. To measure the practical application performance of the designed TME, we applied TME-3 onto the model roofs, clothing surfaces and helmet surfaces, and performed thermal measurements in urban areas, specifically in parks and building complexes.

### Simulation of extraterrestrial cooling performance

To explore the radiative cooling performance of broadband TME-1 in outer space, we used COMSOL Multiphysics to simulate the temperature behaviour of a polar-orbiting satellite operating in low Earth orbit (Supplementary Fig. 41). The satellite model was simplified as a hollow cube with a side length of 50 cm. The outer surface material was set to TME-1 (excluding the antenna), and the frame material was an aluminium alloy. There were two constant-power heat sources inside. The thermal radiation exchange objects of the satellite were the Earth (atmospheric longwave radiation, 3–40 μm), the Sun (solar irradiance was assumed to be under air mass zero) and the Universe (cold source of 4 K). The internal heat conduction of the satellite was automatically set by the software. We calculated the temperature changes at the highest temperature point of the simulation model under different thermal loads (240 and 450 W) and different surface settings. We also explored the stability of TME-1 during service in low Earth orbit, as detailed in Supplementary Fig. 40.

## Data availability

All the data and models used, generated or analysed during the current study are available from the corresponding author H.Z. upon request.

## Code availability

The code used to construct the dataset and for the inverse design of these models is available at Zenodo (https://doi.org/10.5281/zenodo.15229359)[51].

51. Xiao, C. Ultrabroadband and band-selective thermal meta-emitters by machine learning. Code and dataset for inverse design of thermal meta-emitters. *Zenodo* https://doi.org/10.5281/zenodo.15229359 (2025).

**Acknowledgements** H.Z. acknowledges financial support from the National Natural Science Foundation of China (grant 52172120) and the Shanghai Science and Technology Development Funds (grant 24CL2900500). D.Z. acknowledges financial support from the Shanghai Jiao Tong University 2030 Initiative. C.-W.Q. acknowledges financial support from the Ministry of Education, Republic of Singapore (grant A-8002978-00-00), the National Research Foundation, Singapore, under its Medium Sized Centre: Singapore Hybrid-Integrated Next-Generation Electronics Centre funding programme, and the Science and Technology Project of Jiangsu Province (grant BZ2022056). Y. Zheng acknowledges support from the Cullen Trust for Higher Education Endowed Professorship in Engineering No. 4 and Temple Foundation Endowed Teaching Fellowship in Engineering No. 2. M.Y. acknowledges support from the ÅFORSK Foundation (Project 19-512). M.L. acknowledges support from the National Science Foundation of China (grant 52306103). We thank C. Zhou for helpful discussions and suggestions. We thank G. Sun for the helpful discussions on the design of the figures.

**Author contributions** H.Z. and C.X. conceived the idea. H.Z. guided the whole project. C.X. designed the ML framework and performed the finite-difference time-domain calculations. C.X. and K.Y. developed the algorithm and analysed the ML-generated results. C.X. and H.Z. designed the experiments. C.X., M.Z. and Y. Zhang fabricated and characterized the materials. C.X. and X.C. evaluated the energy saving. M.L., K.Y., Y.S., X.L., W.H., T.F., Y.Y., C. Z., Y. Zheng, D.Z. and C.-W.Q. analysed the research data. C.X. and H.Z. wrote the main parts of the manuscript. M.L., K.Y., M.Y., D.Z., Y. Zheng and C.-W.Q. revised the manuscript. All authors discussed the results and commented on the manuscript.

**Competing interests** H.Z. and C.X. have filed intellectual property related to the algorithm. H.Z., C.X., M.Z. and Y. Zhang have filed two patent applications related to the fabrication of this work. The other authors declare no competing interests.

**Additional information**
**Supplementary information** The online version contains supplementary material available at https://doi.org/10.1038/s41586-025-09102-y.
**Correspondence and requests for materials** should be addressed to Yuebing Zheng, Di Zhang, Cheng-Wei Qiu or Han Zhou.
**Peer review information** *Nature* thanks Gil Ju Lee and the other, anonymous, reviewer(s) for their contribution to the peer review of this work.
**Reprints and permissions information** is available at http://www.nature.com/reprints.